Catalysis Today 261 (2016) 67–74

Contents lists available at ScienceDirect

Catalysis Today

journal homepage: www.elsevier.com/locate/cattod

On the kinetics and mechanism of Fischer–Tropsch synthesis on a highly active iron catalyst supported on silica-stabilized alumina

Trent J. Okeson[a], Kamyar Keyvanloo[a], John S. Lawson[b], Morris D. Argyle[a], William C. Hecker[a,*]

[a] Department of Chemical Engineering, Brigham Young University, Provo, UT 84602, United States
[b] Department of Statistics, Brigham Young University, Provo, UT 84602, United States

ARTICLE INFO

Article history:
Received 4 June 2015
Received in revised form 28 August 2015
Accepted 31 August 2015
Available online 2 November 2015

Keywords:
Kinetics modeling
Fischer–Tropsch synthesis
Supported iron
Lack-of-fit test

ABSTRACT

The kinetics of a supported iron Fischer–Tropsch (FT) catalysts were investigated and a physically meaningful model that fits the data very well is proposed. Kinetic data (reported herein) were obtained at 250 °C and 20 atm in a fixed bed reactor at a variety of P_{H_2} and P_{CO}. Measured P_{H_2} and P_{CO} power law dependencies were found to be in the same range as those for unsupported Fe FT catalysts previously reported. The kinetic models in this study were tested using a statistical lack-of-fit test. Eight, two-parameter Langmuir–Hinshelwood rate expressions based on various mechanistic routes and assumptions were derived and tested, but all gave relatively poor fits to the data. An adjustment of the P_{H_2} dependency of the derived expressions to the 0.875 power resulted in three reasonable semi-empirical models, one of which fit the data extremely well. This approach also allowed us to determine the best function of P_{CO} dependency. The results suggest that supported Fe FT catalysts follow a direct CO dissociation pathway, that carbon is one of the most abundant species on the surface of the catalyst, and that the hydrogenation of either C* or CH* is the rate-determining step.

1. Introduction

Fischer–Tropsch (FT) Synthesis (FTS) is a commercially proven and environmentally sound method for production of fuels from natural gas, coal, or biomass. FTS catalysts are typically unsupported iron (Fe) or supported cobalt (Co), each with its own advantages and disadvantages [1]. Although unsupported Fe catalysts, typically promoted with Cu, K, and SiO_2 show promising activity and selectivity [2], they are generally too mechanically weak to be used in slurry bubble column reactors (SBCR's). There is specific interest in using SBCR's because they have excellent heat transfer properties and are very economical [3]. Unfortunately, the severe conditions in SBCR's tend to grind weaker unsupported Fe catalysts into fine powders, resulting in attrition loss with concomitant plugging of catalyst filter systems [4]. Although *supported* Fe catalysts are preferred for SBCR's, historically their activity has been 3–6 times lower than unsupported Fe catalysts and their selectivity has also been less favorable [2,5,6]. However, a highly active and stable silica-stabilized alumina-supported Fe catalyst was recently developed and reported [7,8]. This breakthrough opens new possibilities for supported Fe catalysts and leads to a renewed interest in characterization of supported Fe FTS catalysts, including their kinetic behavior and mechanism.

FTS involves two primary steps: the formation of CH_2 monomers and polymerization of those monomers to form hydrocarbon chains. The majority of kinetic studies are based on the assumption that the formation of the CH_2 monomers is significantly slower than and independent of the polymerization reaction [9]. This simplifies the kinetic analysis to obtain derivable rate equations that describe FTS, allowing for explicit models for monomer formation to be used instead of implicit models that rely on the distribution of products. A selection of proposed rate expressions (based on this assumption) from the literature is shown in Table 1. A more complete review of kinetic studies for Fe FTS catalysts can be found elsewhere [10].

Table 1 includes a power law model, one Eley-Rideal model and three Langmuir–Hinshelwood–Hougen–Watson (LHHW) rate models for unsupported Fe. The last two models are LHHW models for supported Fe. In early FTS research, FTS was assumed to follow an Eley-Rideal type mechanism; now, the LHHW type reaction is

Abbreviations: FT, Fischer–Tropsch; FTS, Fisher-Tropsch Synthesis; SBCR, slurry bubble column reactor; LHHW, Langmuir–Hinshelwood–Hougen–Watson; MASI, most abundant surface intermediate; ΔH_{ads}, heat of adsorption; L.o.F., lack-of-fit; SE, semi-empirical; LCM, linear combination model; MAPM, multiple adsorption parameter model.

* Corresponding author.
E-mail address: hecker@byu.edu (W.C. Hecker).

http://dx.doi.org/10.1016/j.cattod.2015.08.054
0920-5861/

Table 1
Summary of kinetic models of FTS on iron catalysts found in literature.

Catalyst	Reactor	Operating conditions			Kinetic expression	Ref.
		T (°C)	P (MPa)	H_2/CO		
Prec. $FeKAl_2O_3$	Berty CSTR	200–240	1.0	1.0–2.0	$-r_{CO} = aP_{H_2}^{0.6}P_{CO}^{-0.05}$	[11]
Prec. $FeCuSiO_2$	Spinning Basket Reactor	270–330	1.3–2.5	0.5–2.0	$r_{FT} = \frac{aP_{CO}P_{H_2}}{bP_{CO}+cP_{H_2O}}$	[12]
Prec. $FeCuKSiO_2$	Slurry Reactor	250	1.2–4.0	0.5–2.0	$r_{FT} = \frac{aP_{CO}^{1/2}P_{H_2}^{1/2}}{(1+bP_{CO}^{1/2}+cP_{CO_2})^2}$	[13]
FeKZnCu	Packed Bed	235	0.8–2.4	1.0–4.8	$r_{FT} = \frac{aP_{CO}P_{H_2}+bP_{CO}}{(1+cP_{CO})^2}$	[14]
Prec. FeK	CSTR	240	0.5–4.0	1.6	$r_{FT} = \frac{aP_{H_2}^{0.5}P_{CO}}{(1+bP_{CO})^2}$	[15]
$FePt/LaAl_2O_3$	Berty CSTR	220–239	0.5–1.4	1.0–10	$r_{FT} = \frac{aP_{H_2}^{5/6}P_{CO}^{2/3}}{(1+bP_{H_2}^{1/3}P_{CO}^{2/3})^2}$	[16]
$FeKPt/Al_2O_3$	Berty CSTR	220–260	2.0	1.8–14	$-r_{CO} = \frac{aP_{H_2}^{3/4}P_{CO}^{1/2}}{(1+bP_{H_2}^{1/4}P_{CO}^{1/2})^2}$	[17]

generally accepted and is the primary type of mechanism explored in this study [18].

The first model in Table 1 is an example of a power law rate expression for a potassium promoted Fe catalyst. There have been many power law rate expressions proposed for Fe catalysts with varying orders of H_2 and CO. The reported reaction orders with respect to H_2 and CO differ greatly as the catalyst promoters are varied; however, when examining only K promoted iron catalysts, the dependence on H_2 is reported to be between 0.6 and 0.9, while CO dependence varies between −0.2 and 0.2 [11].

In more than a dozen previous studies of reaction kinetics of FTS, only two included the kinetics of supported Fe FT catalysts. In the first study, Critchfield and Bartholomew [16] examined the kinetics of a Pt-promoted (20% Fe, 1% Pt) catalyst supported on a lanthanum-stabilized alumina in a Berty reactor. In the second study, Paul and Bartholomew [17,19] examined the kinetics of FTS on an alumina-supported, K-promoted (20% Fe, 1% K, 1% Pt) catalyst. Rate equations were derived from a variety of mechanistic models and then fit to the data using the Levenberg–Marquardt algorithm for nonlinear least squares regression. Although these studies made good progress in kinetic modeling of supported Fe FT catalysts, they had challenges with deactivation. In addition, the activities of their catalysts were below commercial standards and one included Pt which is not commercially viable.

In summary, the kinetics of supported Fe catalysts have been explored only sparsely. The lack of interest is due to their poor performance relative to unsupported catalysts, which has made supported Fe appear to be commercially unattractive. With the recent development of a potentially competitive supported Fe FTS catalyst [7], kinetic modeling of supported Fe catalysts is now more relevant. In this paper, we explore kinetic rate models that best describe rate data obtained on a highly active, supported Fe catalyst prepared in our laboratory.

2. Experimental

2.1. Catalyst preparation

The catalyst used in this study was iron supported on silica-stabilized alumina (5% silica) promoted with copper and potassium (FeCuK/AlSi). It was prepared using a non-aqueous solution (50 vol% acetone and 50 vol% iso-propanol) containing ferric nitrate and copper nitrate in multiple impregnation steps using a rotary evaporator. In each step, 10 wt% Fe with the desired amount of Cu was dissolved in an appropriate volume of solution followed by drying and calcination at 300 °C. After the last step of Fe and Cu addition, potassium was added by incipient wetness impregnation as potassium bicarbonate. The final catalyst contained nominally 40 wt% Fe, 3 wt% Cu, and 1.6 wt% K and was sieved to a particle size of 125–177 μm (80–120 mesh) to eliminate pore diffusion effects. The detailed catalyst preparation procedure (as well as characterization data) can be found elsewhere [7,8].

2.2. Kinetic data

The kinetic data for FTS were obtained in a fixed-bed reactor (stainless steel, 3/8 in. OD). The catalyst sample (0.25 g) was diluted with 1 g of SiC to provide a nearly isothermal profile throughout the catalyst bed. The catalyst was reduced in situ at 320 °C in H_2 for 16 h. The reactor was then cooled to 180 °C and pressurized to 20 atm in flowing syngas (31.5% CO, 31.5% H_2, 3.5% Ar, balance He). The catalyst was activated at 280 °C for approximately 72 h with a target CO conversion level of 50% during this carburization period. The effluent product passed through a hot trap (~90 °C) and a cold trap (~0 °C) to collect solid and liquid products, respectively. The gaseous product was analyzed using an HP 5890 gas chromatograph. Details of the reactor system can be found elsewhere [20]. The H_2 and CO partial pressures were varied systematically to collect the kinetic rate data. The ranges over which the partial pressures were varied as well as the other operating conditions of this study are shown in Table 2.

Obtaining rate data without being effected by catalyst deactivation is a common challenge in the kinetic modeling of FTS. The Fe catalyst used in this study was very stable, as evidenced by essentially no activity change during the data collection period (200–700 h TOS). As shown in Fig. 1, the variation in rate is minimal, indicating that there is no need to correct data for deactivation.

All the rate data were obtained at low CO conversions (17–21%) and were calculated assuming differential reactor conditions. Average partial pressures of H_2 and CO between inlet and outlet

Table 2
Range of operating conditions for the FeCuK/AlSi catalyst.

Operating conditions	Value
H_2:CO	0.7–1.5
P_{H_2} (atm)	2.0–9.0
P_{CO} (atm)	3.0–8.9
P_{tot} (atm)	20
T (°C)	250
Time on stream (TOS) (h)	200–700
CO conversion	0.17–0.21

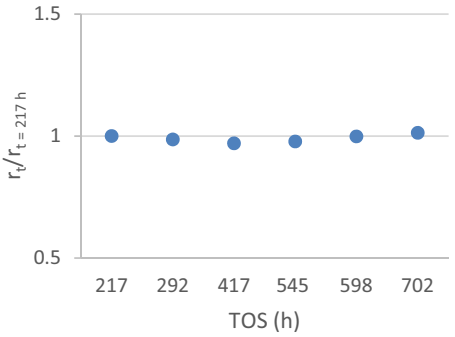

Fig. 1. Normalized activity at $T = 250\,^{\circ}C$, $P_{H_2} = 6.1$ atm, $P_{CO} = 6.2$ atm up to 700 h TOS.

of the reactor were used in the kinetic analysis. Calculations verified the differential assumption, showing less than 1% error when compared to using an integral reactor model.

2.3. Mechanisms

As mentioned previously, LHHW models are typically used in the literature to describe the mechanism for FTS. The mechanistic routes explored in this study are shown in Fig. 2. Both H-assisted and unassisted CO dissociation routes were considered. The direct CO dissociation pathway (step 3) forms C* and O* as intermediates, while subsequent reactions with H* yield CH_2* monomers (steps 4, 10). The O* atoms (formed in step 3) are removed as H_2O via stepwise reactions with H* or as CO_2 via a reaction with CO*. For the H-assisted CO dissociation route, CO* forms formyl intermediates (HCO*) via a reaction with H*. The HCO* then either dissociates directly to CH* and O* or by first forming HCOH*. After dissociation, CH* reacts with H* to form CH_2*, which is the primary monomer required for chain growth. Oxygen is removed as H_2O or CO_2 for unassisted HCO* dissociation; however, for H-assisted HCO* dissociation, oxygen is only removed as H_2O because no O* is formed on the surface (only OH*) via this reaction pathway.

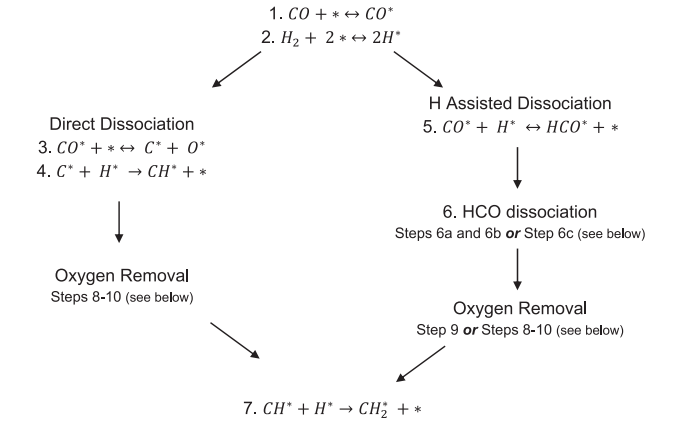

	Oxygen Removal		6. HCO Dissociation
H_2O	8. $O^* + H^* \leftrightarrow OH^* + *$ 9. $OH^* + H^* \rightarrow H_2O + 2*$	H Assisted	a. $HCO^* + H^* \leftrightarrow HCOH^* + *$ b. $HCOH^* + * \rightarrow CH^* + OH^*$
CO_2	10. $CO^* + O^* \rightarrow CO_2 + 2*$	Direct	c. $HCO^* + * \rightarrow CH^* + O^*$

Fig. 2. Flow schematic of possible mechanistic routes for FTS.

2.4. Rate expressions

From the mechanistic steps in Fig. 2, a series of 2-parameter LHHW rate expressions were derived and are shown in Table 3. For brevity, only a subset of the derived rate expressions considered

Table 3
Rate models used in this study including the assumptions made to derive each rate equation.

Kinetic expression		CO dissociation path	Rate limiting step (s)	MASI	Oxygen removal
Power law	$k_1 P_{H_2}^{\alpha} P_{CO}^{\beta}$		Empirical		
Carbide 1	$\frac{k_1 P_{H_2}^{0.5} P_{CO}^{0.5}}{(1 + k_2 P_{CO}^{0.5})^2}$	Direct	4	C*, O*	CO_2
Carbide 2a	$\frac{k_1 P_{H_2}^{0.75} P_{CO}^{0.5}}{(1 + k_2 P_{CO})^2}$	Direct	4	CO*	H_2O
Carbide 2b	$\frac{k_1 P_{H_2}^{0.75} P_{CO}^{0.5}}{(1 + k_2 P_{H_2}^{0.25} P_{CO}^{0.5})^2}$	Direct	4,9	C*	H_2O
Carbide 3	$\frac{k_1 P_{H_2} P_{CO}^{0.5}}{(1 + k_2 P_{CO}^{0.5})^2}$	Direct	7	C*, O*	CO_2
H assisted 1	$\frac{k_1 P_{H_2} P_{CO}}{(1 + k_2 P_{CO})^2}$	H assisted HCO: H assisted	6b	CO*	H_2O
H assisted 2a	$\frac{k_1 P_{H_2} P_{CO}^{0.5}}{(1 + k_2 P_{CO})^2}$	H assisted HCO: H assisted	7	CO*	H_2O
H assisted 2b	$\frac{k_1 P_{H_2} P_{CO}^{0.5}}{(1 + k_2 P_{H_2}^{0.5} P_{CO}^{0.5})^2}$	H assisted HCO: H assisted	7	HC*	H_2O
H assisted 3	$\frac{k_1 P_{H_2}^{0.5} P_{CO}}{(1 + k_2 P_{CO})^2}$	H assisted HCO: direct	5	CO*	CO_2
Botes [21]	$\frac{k_1 P_{H_2}^{0.75} P_{CO}^{0.5}}{(1 + k_2 P_{CO}^{0.5})^2}$	Direct, semi empirical model	NA	NA	NA

in this study are included in this paper. The expressions included in Table 3 were chosen for a variety of reasons (e.g., for physical significance or quality of fit) and are a good overall representation of the all the tested models. The expressions used in this study were derived by varying the reaction pathway, the rate determining step, the most abundant surface intermediates (MASI), and the oxygen removal step(s). In addition to the derived rate expressions, the power law and a semi-empirical expression from the literature are also included. The constants in Table 3 are distinguished between rate constants and equilibrium constants as k and K, respectively. The equilibrium constants arise from the quasi-equilibrium assumption for the adsorption steps and their temperature dependency is $\exp(-\Delta H_{ads}/RT)$. In LHHW models, the ΔH_{ads} is assumed to be independent of coverage to simplify the kinetic modeling. This assumption is discussed in more detail by Botes et al. [21].

2.5. Statistical analysis

Once the data were obtained, the nlsLM function in the R package minpack.lm [22] was used to fit the kinetic rate expressions in Table 3 to the kinetic data of this study. The nlsLM function uses a modified Levenberg–Marquardt fitting algorithm. This function calculates the estimated parameters (rate constants) and other summary statistics, such as the standard error of the estimates, and *P*-values. Two *P*-values are discussed in this work. The first, the parameter *P*-value (labeled $Pr(k_1)$, $Pr(k_2)$ or $Pr(\alpha)$, and $Pr(k_3)$ or $Pr(\beta)$ in Tables 5, 6 and 8), indicates the statistical significance of the estimated parameters. Typically, statistically significant parameters have a *Pr* (*P*-values) less than 0.05, while highly significant parameters have *Pr* values less than 0.01.

To more accurately define how well each model fit the data, lack-of-fit (L.o.F.) tests, were performed by comparing the variability in the differences of the model predictions and the raw data to the variability in raw data obtained at constant conditions. *P*-values for these L.o.F. tests are shown in Tables 5, 7 and 8. An insignificant L.o.F. test (high *P*-value) is favorable for the model and indicates that predictions from the model at a certain set of conditions will be as accurate as performing additional experiments at those conditions. In this paper, models with L.o.F. *P*-values (reported as L.o.F. *P*-value in Tables 5, 7 and 8) greater than 0.10 were assumed to have an insignificant L.o.F., and cannot be ruled out as reasonable models based on their predictions of the data.

While macrokinetic analysis and statistics cannot be used to prove that FTS follows a particular reaction pathway, this method of analysis identifies plausible kinetic pathways and also eliminates invalid models. By looking into the assumptions made for each of the models that are not ruled out due to the L.o.F. test, insights can be gained about the most probable reaction pathways.

3. Results and discussion

3.1. Kinetic data

Rate data for the FeCuK/AlSi catalyst were obtained at the conditions indicated in Table 2 and are shown in Table 4. The FT rate (r_{FT}) in this paper is defined as the rate of consumption of CO plus H_2 ($(-r_{CO})+(-r_{H_2})$) because this combination eliminates the rate of the water–gas shift reaction from the measured rate of CO consumption giving a more accurate representation of the rate of FTS. Multiple data points were collected at a standard condition (6.1 atm H_2, 6.2 atm CO), as can be seen in Table 4 and Fig. 1, and demonstrate excellent repeatability with a variability of less than 3%.

Table 4
Rate data collected in fixed bed reactor at 250 °C.

TOS (h)	P_{CO} (atm)	P_{H_2} (atm)	r_{FT} (mmol/g/h)
217	6.25	6.09	135
245	5.74	3.60	82.6
266	5.79	8.81	183
292	6.22	6.11	133
341	8.50	5.35	108
358	2.84	1.82	54.9
382	2.86	2.89	78.8
400	8.55	8.39	160
417	6.22	6.12	131
545	6.22	6.11	132

3.2. Results for 2-parameter models

The data described in Section 3.1 were fit to a power law model and the nine two parameter rate expressions in Table 3. Kinetic parameters based on best fit values for these rate models along with the standard error (St. error), *Pr* value, L.o.F. *P*-values, and residual mean squares are given in Table 5.

The power law model fit the data very well with a *P*-value of 0.422. With respect to H_2, the reaction order was 0.877, while the order with respect to CO was −0.221. The negative dependence of P_{CO} suggests that either CO or another carbon containing species is an abundant surface intermediate, limiting the sites available for adsorption and reaction. While the power law model fits the data well, it offers little insight into the mechanism and cannot be used to predict the rate at varying reaction temperatures, limiting the value of this model.

The H_2 and CO dependencies found in this power law model are consistent with the values reported for potassium promoted Fe catalysts. The H_2 dependence of 0.877 and CO dependence of −0.221 both fall within the literature reported ranges. This observation would seem to indicate that the kinetics of Fe catalysts as modeled by a power law rate expression are not significantly impacted by adding a support.

None of the 2-parameter models fit the data well. The two best models, Botes and Carbide 2a, had L.o.F. *P*-values of 0.041 and 0.052, respectively, which are well below the 0.10 cut off value we used for statistical significance. To visually confirm the poor fit, the residuals (i.e., the differences between the measured rate data and the model predictions) are shown in Fig. 3(a) and (b) for the Botes and Carbide 2a models, as a function of P_{H_2}. While the residuals for accurate models should be randomly distributed around 0, these data show a clear trend in deviations in error with respect to P_{H_2} as highlighted by the dashed line. This behavior indicates that the model overpredicts the rate at low P_{H_2} and underpredicts the rate at high P_{H_2} resulting in a poor fit of the data. Both CO and H_2 residuals were analyzed, but this trend in rate with P_{H_2} is the primary reason for the poor fit for both of the models.

3.3. Semi-empirical models

The residual plots in Fig. 3 identify that there is an overall trend with the P_{H_2} for both of the best 2-parameter rate models. To better fit the data, semi-empirical models that adjusted the H_2 dependence were explored. The power law fit of the data resulted in a hydrogen power of 0.877 (shown in Table 5), which was approximated as 7/8 or 0.875 for use in the semi-empirical modeling. The semi-empirical models were created by changing the order of hydrogen in the numerator to 0.875 for each of the derived rate expressions in Table 3. This resulted in three semi-empirical models, shown in Table 6, that were the best of the adjusted models tried. SE.I is based on the best model from the non-empirical two parameter models, the Carbide 2a model, or the H-assisted 2a

Table 5
Optimized values of parameters for each of the rate equations obtained by using the nlsLM optimizer and the statistical parameters indicating quality of fit for each of models. The pressures are in atm and the rates are in mmol/g/h. Units for rate constants vary to maintain the stated rate units.

Kinetic expression		k_1 Std. error $Pr(k_1)$	k_2 or α Std. error or $Pr(\alpha)$	β Std. error $Pr(\beta)$	L.o.F. *P*-value	Residual Mean Square
Power law	$k_1 P_{H_2}^{\alpha} P_{CO}^{\beta}$	40.2 1.7E+00 5.4E−08	0.877 2.1E−02 1.1E−04	−0.221 2.8E−02 1.4E−09	0.422	3.62
Carbide 1	$\frac{k_1 P_{H_2}^{0.5} P_{CO}^{0.5}}{(1+k_2 P_{CO}^{0.5})^2}$	36.5 6.7E+00 6.2E−04	0.048 1.9E−02 3.1E−02		0.002	162
Carbide 2a	$\frac{k_1 P_{H_2}^{0.75} P_{CO}^{0.5}}{(1+k_2 P_{CO})^2}$	31.7 2.3E+00 7.0E−07	0.083 8.6E−03 1.6E−05		0.052	17.2
Carbide 2b	$\frac{k_1 P_{H_2}^{0.75} P_{CO}^{0.5}}{(1+k_2 P_{H_2}^{0.25} P_{CO}^{0.5})^2}$	37.4 1.1E+01 7.4E−03	0.167 1.7E−01 2.1E−02		0.002	136
Carbide 3	$\frac{k_1 P_{H_2} P_{CO}^{0.5}}{(1+k_2 P_{CO}^{0.5})^2}$	325 2.0E+02 1.4E−01	2.07 7.4E−01 2.4E−02		0.014	42.7
H assisted 1	$\frac{k_1 P_{H_2} P_{CO}}{(1+k_2 P_{CO})^2}$	39.6 9.2E+00 2.6E−03	0.382 6.3E−02 2.9E−04		0.014	42.7
H assisted 2a	$\frac{k_1 P_{H_2} P_{CO}^{0.5}}{(1+k_2 P_{CO})^2}$	27.9 4.0E+00 1.1E−04	0.128 2.0E−02 2.2E−04		0.013	45.0
H assisted 2b	$\frac{k_1 P_{H_2} P_{CO}^{0.5}}{(1+k_2 P_{H_2}^{0.5} P_{CO}^{0.5})^2}$	26.0 5.7E+00 1.8E−03	0.117 3.0E−02 4.1E−03		0.003	123
H assisted 3	$\frac{k_1 P_{H_2}^{0.5} P_{CO}}{(1+k_2 P_{CO})^2}$	33.9 8.7E+00 4.5E−03	0.157 4.0E−02 4.4E−03		0.002	154
Botes	$\frac{k_1 P_{H_2}^{0.75} P_{CO}^{0.5}}{(1+k_2 P_{CO}^{0.5})^2}$	102.5 2.5E+01 3.6E−03	0.698 1.3E−01 8.4E−04		0.041	20.6

model. The SE.II model is based on the H-assisted 1 or 3 models. The last model, SE.III, is based on the Carbide 1 or 3 models and is similar to the Botes 2 parameter semi-empirical model. The three semi-empirical rate expressions in Table 6 fit the data significantly better than any of the derived rate models, indicating that the fit is highly dependent on the H_2 power.

With a L.o.F. *P*-value of 0.551 and a residual mean square of 2.86 the SE.III model is significantly better than any of the other models examined in this study, including SE.I and SE.II. The only model that approaches similarity in terms of residual mean square and L.o.F. *P*-value is the power law, which has one more parameter and is also not based on any theoretically based rate equations. The 7/8 power of P_{H_2} dependence in these models made a significant difference in the three rate models shown in Table 6. A summary of the improvements in *P*-value can be seen in Table 7. The most significant improvement in *P*-value was seen by adjusting the P_{H_2} dependence of the Carbide 1, Carbide 3, or Botes models. These adjustments to produce the SE.III model increased the L.o.F. *P*-value from less than 0.05 up to 0.551.

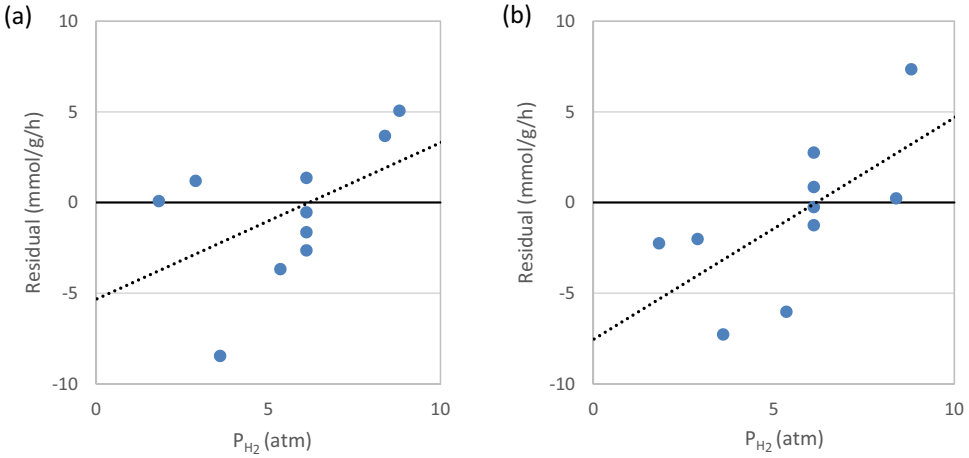

Fig. 3. The residuals of FTS rate (actual – calculated) of the selected kinetic models as a function of the partial pressure of H_2: (a) Botes model and (b) Carbide 2a model.

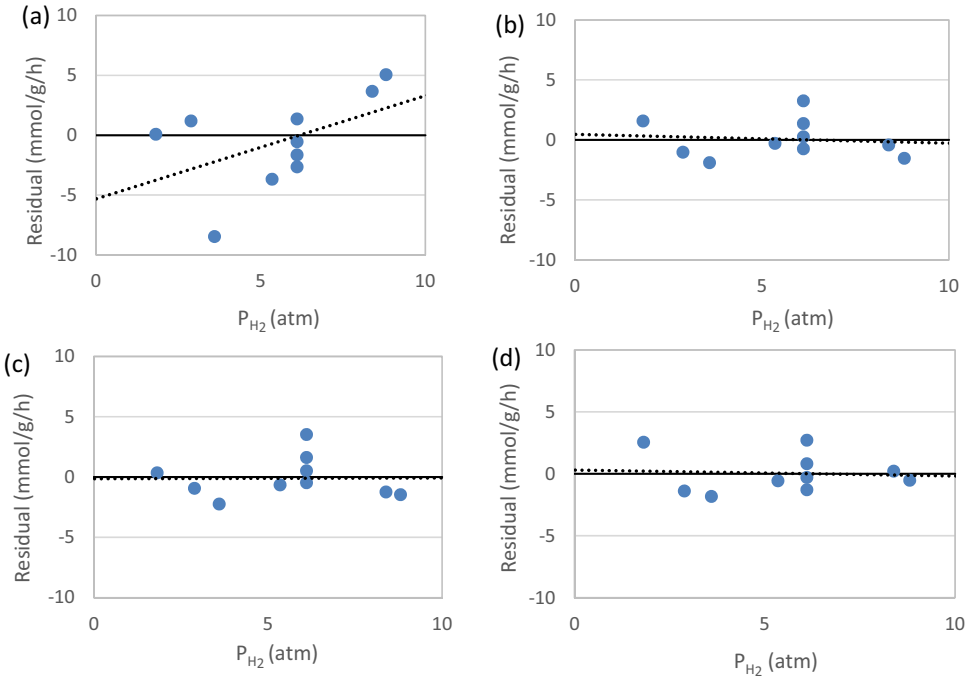

Fig. 4. Residuals of calculated rates versus experimental rates as a function of the H_2 partial pressures in atm. The dotted line is a linear fit of the residuals: (a) Carbide 2a, (b) SE.III, (c) LCM, (d) MAPM.

Table 6
Fitting parameters for the best semi-empirical models from this study and their statistical parameters indicating quality of fit. The pressures are in atm and the rates are in mmol/g/h.

Kinetic expression		k_1 Std. error $Pr(k_1)$	k_2 Std. error $Pr(k_2)$	L.o.F. *P*-value	Residual Mean Square
SE.I	$\frac{k_1 P_{H_2}^{0.875} P_{CO}^{0.5}}{(1+k_2 P_{CO})^2}$	29.7 1.80E+00 1.85E−07	0.104 7.87E−03 1.02E−06	0.109	10.2
SE.II	$\frac{k_1 P_{H_2}^{0.875} P_{CO}}{(1+k_2 P_{CO})^2}$	36.7 3.66E+00 8.33E−06	0.304 2.31E−02 1.05E−06	0.099	10.9
SE.III	$\frac{k_1 P_{H_2}^{0.875} P_{CO}^{0.5}}{(1+k_2 P_{CO}^{0.5})^2}$	158 2.01E+01 4.98E−05	1.13 9.73E−02 2.76E−06	0.551	2.86

Once the P_{H_2} dependency was properly adjusted, a determination of the best CO dependency becomes clearer. Initially, the CO dependency appeared to be best represented by Eq. (1), which was based on the Carbide 2a model. This conclusion was misleading, however, because the dependency was skewed by inaccurate modeling of the H_2 dependency. From the semi-empirical models, it becomes clear that the CO dependency is best represented by Eq. (3). Thus, with an accurate P_{H_2} dependency, the comparison of the CO dependency becomes clearer.

$$f_1(P_{CO}) = \frac{aP_{CO}^{0.5}}{(1+bP_{CO})^2} \quad (1)$$

$$f_2(P_{CO}) = \frac{aP_{CO}}{(1+bP_{CO})^2} \quad (2)$$

$$f_3(P_{CO}) = \frac{k_1 P_{CO}^{0.5}}{(1+k_2 P_{CO}^{0.5})^2} \quad (3)$$

Table 7
Summary of the relationship between derived and semi-empirical (adjusted) models.

Initial Model	L.o.F. *P*-value	Adjusted model	L.o.F. *P*-value	P_{CO} dependency
Carbide 2a H-assisted 2a	0.052 0.013	SE.I	0.109	f_1
H-assisted 1 H-assisted 3	0.014 0.002	SE.II	0.099	f_2
Carbide 1 Carbide 3 Botes	0.002 0.014 0.041	SE.III	0.551	f_3

3.4. Three-parameter models

The SE.III model accurately predicts the rate of FT for our supported Fe catalyst; however, the insight into the mechanism gained from this model is limited because it is semi-empirical. To gain more insight into the mechanism, three-parameter models that had similar dependencies to the SE.III model were derived. The SE.III model was used to suggest two theoretically based three-parameter models. One method of obtaining an overall H_2 power of 0.875 is a linear combination of two rate laws with hydrogen

Table 8
Fitting parameters three-parameter models and their statistical parameters indicating quality of fit. The pressures are in atm and the rates are in mmol/g/h.

Kinetic expression		k_1 Std. error $Pr(k_1)$	k_2 Std. error $Pr(k_2)$	k_3 Std. error $Pr(k_3)$	L.o.F. *P*-value	Residual Mean Square
LCM	$\frac{k_1 P_{H_2}^{0.5} P_{CO}^{0.5} + k_2 P_{H_2} P_{CO}^{0.5}}{(1 + k_3 P_{CO}^{0.5})^2}$	69.3 9.60E+00 1.74E−04	83.4 1.80E+01 2.40E−03	1.04 1.30E−01 9.01E−05	0.401	3.65
MAPM	$\frac{k_1 P_{H_2}^{0.75} P_{CO}^{0.5}}{(1 + k_2 P_{H_2}^{0.25} P_{CO}^{0.5} + k_3 P_{H_2}^{-0.25} P_{CO}^{0.5})^2}$	207 3.72E+01 8.39E−04	0.256 2.80E−02 3.89E−05	1.19 1.66E−01 1.78E−04	0.479	3.16

powers between 0.5 and 1 that will return the desired overall power. Iglesia and coworkers [14] recently found that a linear combination model resulted in a significantly better fit and suggested that FTS on iron catalysts followed parallel reaction mechanisms. To obtain this combination of two derived rate laws, the Carbide 1 and Carbide 3 mechanisms, were combined. These models were chosen because they had MASI's consistent with the SE.III model. The result for this linear combination model (LCM) is shown as the first entry in Table 8.

A second rate expression derivation that results in the possibility of an overall H_2 power of 0.875 is obtained by assuming multiple adsorption terms with hydrogen dependencies. Botes et al. [21] suggested a three-parameter model that has multiple adsorption species for an industrial *cobalt* catalyst. This was found to be an excellent fit for our supported iron catalyst as well and is also included in Table 8. This multiple adsorption parameter model (MAPM) fit the data slightly better than the LCM, as shown by the L.o.F. *P*-value and the residual mean square, but neither fit the data quite as well as the SE.III model; however, both of these three-prameter models fit the data well enough that they cannot be excluded solely based on statistical analysis. Several other three-parameter models were also tested, but none resulted in L.o.F. *P*-values better than 0.30.

The L.o.F. *P*-values are lower and the residual mean square values are higher for the three-parameter models because these statistical measures take into account the number of parameters in the model. With more parameters, it takes a significantly better fit to get the same *P*-value. Unfortunately, a limited number of data points and high degree of parity between SE.III and the two 3 parameter models makes it impossible to statistically differentiate between these three models with certainty. Residual plots and parity plots are shown in Figs. 4 and 5 respectively for these three models ((b), (c), and (d)) compared to the best derived 2 parameter model, the Carbide 2a model (a). There is a very slight trend in the residuals for the SE.III and MAPM models, but this trend is not significant. In all cases, the LCM, MAPM, and SE.III models produce significantly better fits than the Carbide 2a model. Additionally, these models fit the data very poorly when only two of the parameters are used. For example, in the MAPM if the k_2 term is dropped and the model is refit, the resulting L.o.F. *P*-value is 0.004. Likewise, if the k_3 term is dropped, the L.o.F. *P*-value is 0.002.

3.5. Analysis of three-parameter models

There are several inferences that can be drawn from the LCM, MAPM, and SE.III models. First, all of these rate equations are based on carbide models, suggesting that the preferred mechanistic route for CO dissociation on supported iron catalysts is direct dissociation. Secondly, the MASI's can be compared to understand the surface species found on the catalyst.

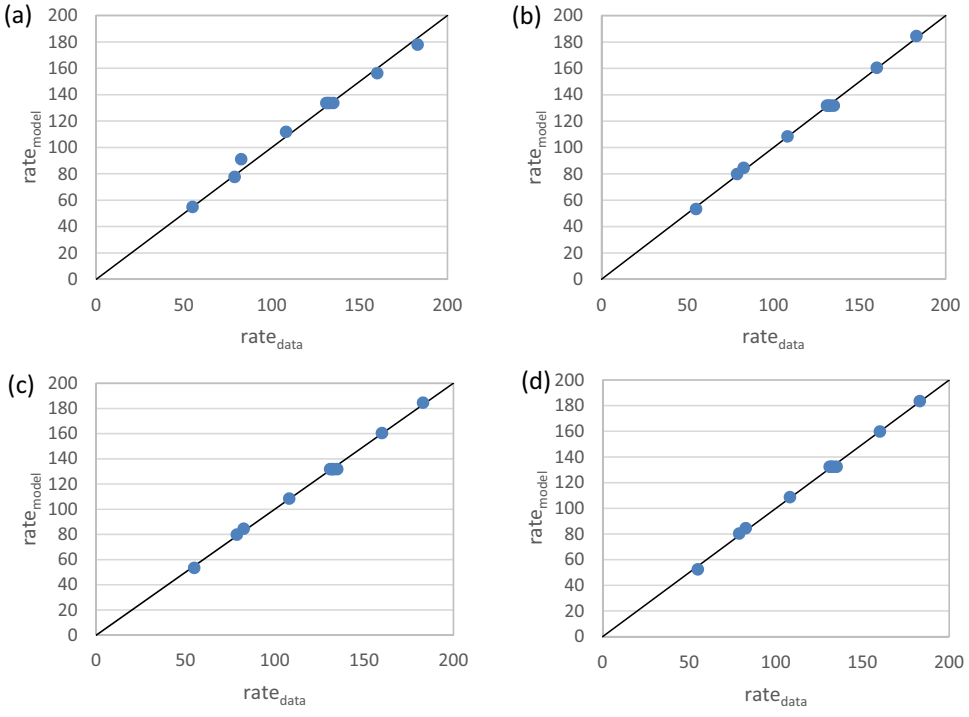

Fig. 5. Accuracy of select kinetic models using parameters shown in Tables 4, 5 and 6: (a) Carbide 2a, (b) SE.III, (c) LCM, (d) MAPM. All rates are in units mmol/g_{cat}/h.

The SE.III and the LCM models were very similar. They both have the same denominator term, $kP_{CO}^{0.5}$, which corresponds to C* and O* being the MASI, suggesting that these are the primary species found on the surface of the catalyst. These species are more likely found on the surface of the catalyst in direct dissociation models, supporting the theory that the CO dissociation mechanism for this supported Fe catalyst is direct dissociation. In the LCM, the assumed rate limiting steps are the first and second hydrogenation steps of C* and CH* to CH* and CH_2*, respectively (steps 4 and 7 in Fig. 2). The first numerator term with $P_{H_2}^{0.5}$ corresponds to the Carbide 1 model. This model assumed that the irreversible rate determining step is the hydrogenation of C* to CH*. The numerator term with P_{H_2} comes from the Carbide 3 model. This model was derived assuming that the rate determining step is the hydrogenation of CH* to CH_2*. Upon rearranging this model to Eq. (4), it can be seen that it has the same P_{CO} dependency as shown in Eq. (3).

$$rate_{FT} = (k_1 P_{H_2}^{0.5} + k_2 P_{H_2}) \frac{P_{CO}^{0.5}}{(1 + k_3 P_{CO}^{0.5})^2} \quad (4)$$

Although there are more differences between the MAPM and SE.II than between LCM and SE.III, there are still several similarities. This model can be derived by two methods using direct dissociation paths. The first method assumes the first hydrogenation of carbon and the second hydrogenation step of oxygen are the rate limiting steps (steps 4 and 9 in Fig. 2). The most abundant species are assumed to be C* and O*, which is consistent with the LCM and SE.III model. The other possible mechanism is that the second hydrogenation of carbon to CH_2* and the first hydrogenation of oxygen are the rate determining steps (steps 7 and 8 in Fig. 2). The MASI for this mechanism are CH* and C*. This mechanism assumes that the hydrogenation steps are slow and rate determining, similar to the LCM. All of these models assumed that C* was a MASI, suggesting that carbon coverage on the surface of the catalyst is high. It is unclear whether O* or CH* is also prevalent on the surface. These observations about the potential MASI's are consistent with the power law findings that suggest that carbon containing intermediates cover the surface, limiting available sites for H_2 dissociation on the catalyst. This model also has the same dependence on P_{CO} as the LCM and the SE.III models and can be seen when the hydrogen terms in the denominator are grouped, as seen in Eqs. (5) and (6).

$$rate_{FT} = k_1 P_{H_2}^{0.75} \frac{P_{CO}^{0.5}}{(1 + f_{H_2} P_{CO}^{0.5})^2} \quad (5)$$

$$f_{H_2} = k_2 P_{H_2}^{0.25} + k_3 P_{H_2}^{-0.25} \quad (6)$$

The biggest difference between the three-parameter models is the oxygen rejection mechanism. The LCM is based on mechanisms that assume O* is eliminated by forming CO_2. The MAPM assumes that oxygen is removed by hydrogenation to form H_2O. However, the water–gas shift (WGS) reaction is fast on iron catalysts, so either removal method can still result in CO_2 being the final product, keeping all models consistent with the data.

4. Conclusions

A kinetic study was performed on a highly active and stable supported Fe catalyst at 250 °C and various P_{H_2} and P_{CO}. The kinetic data obtained were unaffected by catalyst deactivation, as there was essentially no activity change during the data collection period (500 h). The L.o.F. statistical test, novel to kinetic modeling, was used to determine the quality of fit. The P_{H_2} and P_{CO} power law dependencies were determined and indicate that the overall kinetics of supported and unsupported Fe FTS catalysts are similar. The data were also fit to a variety of derived two-parameter models, all of which failed to accurately model the data. Good fits were obtained by using semi-empirical models that corrected the P_{H_2} dependency to 0.875. Once this was done, the CO dependency became clear and is well represented by $f_3(P_{CO}) = k_1 P_{CO}^{0.5}/(1 + k_2 P_{CO}^{0.5})^2$, which includes a half order dependence on P_{CO} in the numerator. The SE.III model ($r_{FT} = k_1 P_{H_2}^{0.875} P_{CO}^{0.5}/(1 + k_2 P_{CO}^{0.5})^2$), the best fitting model, was explained physically by exploring derivable three-parameter models that were consistent with the CO dependency of f_3 and a H_2 dependency of 0.875. The two successful three-parameter models had several key similarities, resulting in the following conclusions from this study: for supported Fe FTS catalysts (1) the dominant mechanism of CO dissociation is unassisted as opposed to H-assisted, (2) carbon is the MASI, and (3) the hydrogenation of C* and/or CH* are/is the rate determining step(s) which results in the high (0.875) observed P_{H_2} dependency.

Acknowledgements

The financial support for this work was provided by members of the Brigham Young University Fischer–Tropsch Consortium and the University of Wyoming Clean Coal Technologies Program. Appreciation is expressed to the members of the Brigham Young University Catalysis Group for technical assistance in this work. Special appreciation is expressed to Jonathon Horton for his early extensive research to develop a kinetic model for our iron catalyst.

References

[1] F.G. Botes, J.W. Niemantsverdriet, J. van de Loosdrecht, Catal. Today 215 (2013) 112–120.
[2] D.B. Bukur, C. Sivaraj, Appl. Catal. A: Gen. 231 (2002) 201–214.
[3] C.H. Bartholomew, Chapter 5. Recent Developments in Fischer–Tropsch Catalysis, in: L. Guczi (Ed.), Studies in Surface Science and Catalysis, Elsevier, 1991, pp. 158–224.
[4] K. Jothimurugesan, J.G. Goodwin Jr., S.K. Gangwal, J.J. Spivey, Catal. Today 58 (2000) 335–344.
[5] R.J. O'Brien, L. Xu, S. Bao, A. Raje, B.H. Davis, Appl. Catal. A: Gen. 196 (2000) 173–178.
[6] J. Xu, C. Bartholomew, J. Sudweeks, D. Eggett, Top. Catal. 26 (2003) 55–71.
[7] K. Keyvanloo, M.K. Mardkhe, T.M. Alam, C.H. Bartholomew, B.F. Woodfield, W.C. Hecker, ACS Catal. 4 (2014) 1071–1077.
[8] K. Keyvanloo, W.C. Hecker, B.F. Woodfield, C.H. Bartholomew, J. Catal. 319 (2014) 220–231.
[9] G.P. van der Laan, A.A.C.M. Beenackers, Appl. Catal. A: Gen. 193 (2000) 39–53.
[10] F.G. Botes, Catal. Rev. 50 (2008) 471–491.
[11] S.A. Eliason, C.H. Bartholomew, Appl. Catal. A: Gen. 186 (1999) 229–243.
[12] A.N. Pour, M.R. Housaindokht, J. Zarkesh, M. Irani, E.G. Babakhani, J. Ind. Eng. Chem. 18 (2012) 597–603.
[13] G.P.v.d. Laan, Kinetics, Selectivity and Scale Up of the Fischer–Tropsch Synthesis, University of Groningen, Netherlands, 1999, pp. 251.
[14] M. Ojeda, R. Nabar, A.U. Nilekar, A. Ishikawa, M. Mavrikakis, E. Iglesia, J. Catal. 272 (2010) 287–297.
[15] F.G. Botes, B.B. Breman, Ind. Eng. Chem. Res. 45 (2006) 7415–7426.
[16] B.L. Critchfield, Statistical Methods for Kinetic Modeling of Fischer Tropsch Synthesis on a Supported Iron Catalyst, Department of Chemical Engineering, Brigham Young University, 2006, pp. 127.
[17] U.P. Paul, Microkinetic Model of Fischer–Tropsch Synthesis on Iron Catalysts, Department of Chemical Engineering, Brigham Young University, 2008, pp. 247.
[18] F.G. Botes, Catal. Rev.: Sci. Eng. 50 (2008) 471–491.
[19] U. Paul, Microkinetic Model of Fischer–Tropsch Synthesis on Iron Catalysts, Chemical Engineering, Brigham Young University, Provo, 2008.
[20] K.M. Brunner, Novel Iron Catalyst and Fixed-Bed Reactor Model for the Fischer–Tropsch Synthesis, Brigham Young University, Provo, UT, 2012.
[21] F.G. Botes, B. van Dyk, C. McGregor, Ind. Eng. Chem. Res. 48 (2009) 10439–10447.
[22] R.D.C. Team, The R Project for Statistical Computing, R Foundation for Statistical Computing, Vienna, Austria, 2014.